Lawrence Berkeley National Laboratory
Energy Storage & Distributed Resources

Title
Alloying ZnS in the hexagonal phase to create high-performing transparent conducting materials

Permalink
https://escholarship.org/uc/item/8bc1t53k

Journal
Physical Chemistry Chemical Physics, 18(32)

ISSN
0956-5000

Authors
Faghaninia, Alireza
Bhatt, Kunal Rajesh
Lo, Cynthia S

Publication Date
2016-08-10

DOI
10.1039/c6cp01278g

Peer reviewed

eScholarship.org Powered by the California Digital Library
University of California

Journal Name

ARTICLE TYPE

Cite this: DOI: 10.1039/xxxxxxxxxx

Alloying ZnS in the hexagonal Phase to Create High-Performing Transparent Conducting Materials

Alireza Faghaninia,[a] Kunal Rajesh Bhatt,[b] and Cynthia S. Lo*[a]

Received Date
Accepted Date

DOI: 10.1039/xxxxxxxxxx

www.rsc.org/journalname

Alloyed zinc sulfide (ZnS) has shown promise as a relatively inexpensive and earth-abundant transparent conducting material (TCM). Though Cu-doped ZnS has been identified as a high-performing p-type TCM, the corresponding n-doped ZnS has, to date, been challenging to synthesize in a controlled manner; this is because the dopant atoms compete with hole-inducing zinc vacancies near the conduction band minimum as the most thermodynamically stable intrinsic point defects. We thus aim to identify the most promising n-type ZnS-based TCM, with the optimal combination of physical stability, transparency, and electrical conductivity. Using a new method for calculating the free energy of both the sphalerite (cubic) and wurtzite (hexagonal) phases of undoped and doped ZnS, we find that doped ZnS is more stable in the hexagonal structure. This, for the first time, fundamentally explains previous experimental observations of the coexistence of both phases in doped ZnS; hence, it profoundly impacts future work on sulfide TCMs. We also employ hybrid density functional theory calculations and a new carrier transport model, AMSET (*ab initio* model for mobility and Seebeck coefficient using the Boltzmann transport equation), to analyze the defect physics and electron mobility of the different cation- (B, Al, Ga, In) and anion-doped (F, Cl, Br, I) ZnS, in both the cubic and hexagonal phases, at various dopant compositions, temperatures, and carrier concentrations. Among all doped ZnS candidates, Al-doped ZnS (AZS) exhibits the highest dopant solubility, largest electronic band gap, and highest electrical conductivity of $3830, 1905,$ and 321 S$\cdot$cm^{-1}, corresponding to the possible carrier concentrations of $n = 10^{21}, 10^{20},$ and 10^{19} cm^{-3}, respectively, at the optimal 6.25% dopant concentration of Al and the temperature of 300 K.

1 Introduction

Transparent conducting materials (TCMs) are an integral component of optoelectronic devices, including thin film solar cells and LCD displays, and increasing efforts have been devoted to identifying, synthesizing, and characterizing inexpensive, earth-abundant, and nontoxic materials for these purposes. Currently, toxic cadmium-based compounds dominate the window layers in inorganic thin film photovoltaics, and the small band gap (e.g., 2.4 eV for CdS) limits the transparency of these materials. Therefore, there is great interest in searching for alternatives that can also provide variability in band alignment and energy level matching[1], which can then be rewarded by improving transmission characteristics and enhancing the PV efficiency ([2]). For example, n-doped zinc oxide (ZnO), including Al-doped (AZO)[3,4], F-doped[5], and Si-doped[6], has shown promise for widespread adoption, as the the highest reported conductivities of ZnO films are in the range of $5000-7000$ S/cm and the highest reported Hall mobilities are about 60 cm^2/V$\cdot$s[7]. Also the carrier concentrations of AZO samples have been reported to be $1.8\times10^{20}-1.0\times10^{21}$ [8,9]. However, defect-driven Fermi level pinning and unintentional n-type conductivity in ZnO makes p-type doping difficult[10]. Nevertheless, the possibility of both n- and p-doping of the same material would confer a competitive advantage in device fabrication, much as it does for silicon. Therefore, developing a comprehensive understanding of the defect physics of alternative wide-gap semiconductors is crucial for TCM design.

Even though zinc sulfide (ZnS) has a similar electronic structure to, but with a higher band gap than, ZnO, it has only recently been identified as a potential host for dopant atoms to increase conductivity. The use of sulfur over oxygen reduces the

[a] *Department of Energy, Environmental, and Chemical Engineering, Washington University, St. Louis, Missouri 63130, USA. E-mail: clo@wustl.edu*
[b] *Department of Energy Science and Engineering, Indian Institute of Technology Bombay, Powai, Mumbai 400 076, India*
† Electronic Supplementary Information (ESI) available: We compare the energy of formation of Al and its bond lengths in ZnS and ZnO. Also, we show how Al affects the density of states at the bottom of the conduction band minimum in ZnS. See DOI: 10.1039/b000000x/

problems associated with the localized character of the ZnO valence band, which is formed by O 2p orbitals[11]; instead, the incorporation of sulfur could delocalize the valence band minimum (VBM), lower the VBM effective mass, and potentially increase the hole mobility. Indeed, several such materials have recently been synthesized and characterized. Cu-doped ZnS has also shown promising characteristics, as it was recently shown to exhibit the best reported hole conductivity and optical transparency for a room temperature-deposited p-type TCM[12,13]; pairing this with n-doped ZnS may result in many promising device applications for photovoltaics, optoelectronics and transparent devices[14]. Traverse et al.[2] enhanced the efficiency of thin film organic solar cells by introducing ZnS co-deposited with Al_2S_3; they reported that the wide band gap hexagonal zinc sulfide (ZnS) ($E_g = 3.7$ eV) can be a good alternative to conventional materials as the anodic buffer layer in OPVs and IGS-based PVs, as it can be thermally deposited in a vacuum environment. Using chemical bath deposition (CBD), Long et al.[15], grew ZnS doped with $0-4\%$ In. Jrad et al.[16], Liao et al.[17] and Nagamani et al.[18] have all grown 0-10% Al-doped ZnS (AZS). Relatively high values of electrical resistivity – on the orders of 10^{3-5} $\Omega \cdot$cm – are reported in these studies for AZS. However, Prathap et al.[19] reported that polycrystalline AZS samples grown by a chemical precipitation method exhibit resistivities as low as 24 $\Omega \cdot$cm at the optimal 6% concentration of Al.

To better understand and control the properties of doped ZnS, we take a closer look at the possible phases and potential structural transformations upon doping. Previous studies[15–19] have largely focused on the cubic polymorph of ZnS, although there are differences in the XRD patterns of their samples. However, a few researchers considered the hexagonal polymorph as well. Hichou et al.[20] observed a polycrystalline mixture of both cubic (β) and hexagonal (α) phases in their samples, as grown by spray pyrolysis techniques. Heiba et al.[21] reported coexistence of the cubic and hexagonal phases in doped ZnS. Deepa et al.[22] reported hexagonal undoped ZnS and hexagonal Co-doped ZnS prepared via chemical bath deposition, with varying crystallinity as a function of dopant concentration. Nevertheless, the lack of discussion on the fundamental and compelling reasons for the phase shift undergone by doped ZnS motivates us to probe the electronic structure of these materials.

In this study, we employ density functional theory (DFT) and AMSET (*ab initio* model for calculation of Mobility and SEebeck coefficient using Boltzmann Transport equation)[23] to analyze the defect physics and screening of different cation and anion alloyed ZnS as candidates for n-type TCMs. Our hypothesis is that there exists an ideal composition of alloyed ZnS, which results in optimal transparent conducting behavior, as outlined above. We use DFT and phonon calculations to calculate the defect formation energy and the phase stability of ZnS alloyed with B, Al, Ga, In, F, Cl, Br and I, and propose Al as the most promising candidate. Also, using *ab inbitio* thermodynamic calculations, we show that the hexagonal phase (wurtzite) of ZnS is more thermodynamically favorable, compared to the cubic (sphalerite) phase, upon doping over a wide temperature range. Finally, we calculate the theoretical limits for electrical conductivity of single crystalline AZS at different carrier concentrations and temperatures. The aim is that the integration of density functional theory calculations, *ab initio* thermodynamics, and electronic transport models can be leveraged to search for high-performing, yet inexpensive, transparent conductors that may one day become the commercial standard.

2 Methods

In order to calculate the electrical drift mobility, we use AMSET[23], which explicitly solves the Boltzmann transport equation (BTE) using Rode's iterative method[24] to obtain the electron distribution in response to a small electric field. We do not use either the variable or constant relaxation time approximation (RTA) in solving the BTE. This enables us to account both for elastic and inelastic scattering mechanisms, such as ionized impurity and polar optical phonon, respectively. Therefore, the prediction of the change in electrical conductivity with temperature or carrier concentration is quite accurate[23]. The general form of the electron distribution remains the equilibrium Fermi-Dirac distribution in response to a small electric field. We can then write:

$$f(\varepsilon) = f_0(\varepsilon) + g(\varepsilon) \tag{1}$$

where f is the actual distribution of the electrons including both elastic and inelastic scattering mechanisms, f_0 is the equilibrium Fermi-Dirac distribution, and $g(\varepsilon)$ is the perturbation to the distribution caused by the small driving force. After calculating g, the mobility can be calculated by integrating the perturbation, the electronic density of state, D_S and group velocity of electrons, v, over energy (Equation 2):

$$\mu = \frac{1}{3E} \frac{\int v(\varepsilon) D_S(\varepsilon) g(\varepsilon) d\varepsilon}{\int D_S(\varepsilon) f(\varepsilon) d\varepsilon} \tag{2}$$

The details of this methodology, as well as its validation with experimental data on GaAs and InN, can be found elsewhere[23].

For each composition of ZnS alloyed with B, Al, Ga, In, F, Cl, Br and I, the geometry of the unit cell is optimized, and the density of states, total energy and band structure are calculated. We use Kohn-Sham density functional theory (KS-DFT)[25,26], as implemented in the Vienna *ab initio* Simulation Package (VASP)[27–30]. The generalized gradient approximation of Perdew, Burke, and Ernzerhof (GGA-PBE)[31] is used to express the exchange-correlation potential, and Projector Augmented Wave (PAW) potentials[32,33] are used to represent the valence wavefunctions. The initial structures are obtained from the ICSD and Materials Project[34,35]. Upon geometry optimization, the lattice constant of the cubic phase increases by 0.6%, and hexagonal phase increases by 2.4%. We then create a $2 \times 2 \times 2$ supercell, containing 32 zinc and 32 sulfur atoms ($Zn_{32}S_{32}$ for the cubic phase and $Zn_{16}S_{16}$ for the hexagonal phase). We simulate alloying by replacing Zn atoms with M in the supercell, or simply, $M_nZn_{32-n}S_{32}$ ($n \in \{0,1,2,3,4\}$) for the cubic phase and $M_nZn_{16-n}S_{16}$ ($n \in \{0,1,2\}$) for the hexagonal phase; M can be B, Al, Ga, or In. Similarly for anion doping, S atoms are replaced with A, where A can be F, Cl, Br or I. Since Zn only has one occupation site in the cubic cell and two in the hexagonal cell,

This journal is © The Royal Society of Chemistry [year]

it does not matter which of the Zn atoms are replaced with the dopant atom. We confirmed this by examining all 32 Zn sites for the cubic supercell and all 16 Zn sites for the hexagonal supercell, when replaced by an Al site. The maximum difference in the energy of all the configurations was 4.8×10^{-9} eV/atom and 2.2×10^{-6} eV/atom, respectively, for cubic and hexagonal phases. Therefore, only the atom at the center resulting in the energy minimum is replaced by different dopant atoms to generate the defect formation energy plots. For higher concentrations of dopants, particularly for Al for which mobility calculations are also performed, we examined all 31 of the possible sites for the second Al dopant and performed geometry optimizations on these configurations. This is necessary because the symmetry is broken upon introduction of the first dopant. We then selected the system with the minimum energy representing 3.125% doping for the cubic cell and 6.25% doping for the hexagonal cell. The difference between the maximum and minimum energy of these configurations is 0.003 eV/atom for the cubic cell and 0.01 eV/atom for the hexagonal cell.

The energy cutoff for the plane wave basis set is set to 520 eV. We choose a k-point mesh of $4 \times 4 \times 4$ for DOS calculations, since the supercell is sufficiently large that increasing the k-point mesh to $6 \times 6 \times 6$ results in less than 0.01 eV difference in the total energy. The non-self consistent energy calculations are performed in a special k-point mesh around the Γ point, at which the CBM occurs in the direct band gap ZnS and all the alloyed ZnS compounds. This k-point mesh contains a total of 992 k-points (for unit cell GW calculations) and 391 k-points (for supercell DFT calculations) in the Irreducible Brillouin Zone (IBZ), with adaptive mesh spacing, to completely account for band anisotropy while remaining dense enough around the Γ point to obtain accurate group velocity and effective mass values.

In order to calculate the group velocities, $v(k)$, and the overall average effective mass, m^*, we fit high-order polynomials to the calculated conduction band around the CBM, with $R^2 > 0.99$. After polynomials are carefully fitted to the conduction band calculated *ab initio*, $v(k)$ and m^* are calculated using Equations 3 and 4, respectively:

$$v(k) = \frac{1}{\hbar}\frac{\partial \varepsilon}{\partial k} \quad (3)$$

$$m^* = \left(\frac{1}{\hbar^2}\frac{\partial^2 \varepsilon}{\partial k^2}\right)^{-1}\Bigg|_{at\ k=0} \quad (4)$$

It should be noted that we calculate m^* only to determine its changes with composition together with changes in overall electrical mobility. Therefore, careful and accurate calculation of the value of the effective mass itself is not the main goal of this study, as it does not appear in the full band formulation of AMSET. All phonon calculations are performed using the Phonopy code[36]. The list of parameters that have been used in AMSET for mobility calculations are provided in Table 1. We assume constant deformation potential, dielectric, elastic and piezoelectric constants for all systems, since mobility is less sensitive to these parameters than the band structure, density of states and optical phonon frequencies[23]. While we used the experimental values[24] for the

Table 1 Inputs to AMSET, as calculated *ab initio* and/or measured experimentally. The bolded numbers are used in the present calculations.

Parameter	*ab initio*	Experimental[24]
PO phonon frequency, ω_{po} (THz)	**9.5±0.2**	10.6
Low-frequency dielectric constant, ε_0	—	**8.32**
High-frequency dielectric constant, ε_∞	—	**5.13**
Deformation potential, E_D (eV)	—	**4.9**

dielectric constants, they could, in principle, be calculated *ab initio* using DFPT. One value for PO-phonon frequency is reported in Table 1, along with the range in calculated values, as obtained using DFT for undoped ZnS. The larger dopant atoms reduce the frequency down to 9.3 THz (e.g., by I) while the smaller ones increase the frequency up to 9.7 THz (e.g., by B).

In order to calculate the formation energy of the defects, we use Equation 5:

$$\Delta H_f(D,q) = E_{tot}(D,q) - E_{tot}(I,0) - \sum_i \Delta n_i(E_i + \Delta\mu_i) + qE_F \quad (5)$$

where $E_{tot}(D,q)$ and $E_{tot}(I,0)$ are the total energies of the defective (e.g. $Zn_{31}S_{32}$ for simulating a zinc vacancy) and ideal supercell (i.e. $Zn_{32}S_{32}$), respectively, as calculated using the HSE hybrid functional. E_i is the energy of bulk element i and Δn_i is the change in its numbers, q is the charge state of the defect, E_F is the value of the Fermi level (i.e., the sum of valence band maximum and relative Fermi level), and the chemical potential, $\Delta\mu_i$, is determined by the growth conditions. Many possible intermediate phases can be formed by the dopants together with either Zn or S atoms. We assume that the dopants are present in their elemental form (i.e., no secondary phases form). Therefore, as an example, under Zn-rich conditions, the chemical potential of Zn is assumed to be 0, while that of S is $\Delta\mu_{\mathrm{S}} = \Delta H_{f,\mathrm{ZnS}} = -1.63$ eV; also, $\Delta\mu_{Al} = 0$. However, under S-rich conditions, $\Delta\mu_{\mathrm{Zn}} = \Delta H_{f,\mathrm{ZnS}} = -1.63$ eV and $\Delta\mu_{\mathrm{S}} = 0$, but the chemical potential of Al should be equal or lower than formation of the most stable intermediate phase; therefore, $\Delta\mu_{\mathrm{Al}} = \frac{1}{2} \times \Delta H_{f,\mathrm{Al_2S_3}} = -2.75$ eV. Similarly, we have determined the chemical potential of B, Ga, In, F, Cl, Br and I considering the following phases: BS_2, B_2S_3, $B_{12}S$, Al_2S_3, GaS, Ga_2S_3, InS, In_5S_4, In_2S_3, In_6S_7, In_3S_4, ZnF_2, $ZnCl_2$, $ZnBr_2$, and ZnI_2. The data for the energy of these phases have been extracted from Materials Project[34,35] via an in-house automated Python code which uses pymatgen[37]. The energy correction of Makov and Payne[38] is also used to minimize the effect of charge self interaction under periodic boundary conditions. More details on the methodology for defect formation energy calculations are available elsewhere[39]. We use these calculations to quickly screen many defects at different charge states to identify the competing and relevant defects and dopants. Furthermore, we perform a more extensive *ab initio* thermodynamic calculations in the framework used by Jackson and Walsh[40]. We calculate the vibrational contribution to the entropy (Gibbs free energy) of alloyed ZnS at relevant temperatures (i.e., room temperature and higher). The zero temperature contribution to the Gibbs energy is calculated using DFT and the GGA-PBE functional, and the non-

zero temperature contribution is calculated via Phonopy[36]. Our calculations of the phonon band structure and density of states agree well with the literature[41]. These calculations are crucial for identifying the thermodynamically most favorable phases of ZnS, before and after doping, at physically relevant temperatures. The details of the calculations are also available elsewhere[42].

3 Results and Discussion

3.1 Thermodynamic Stabilities

First, to calculate the stability of the dopant candidates, we calculated the enthalpy of formation of intrinsic defects, such as the zinc vacancy, V_{Zn} and sulfur vacancy, V_{Zn}. Furthermore, the extrinsic cation dopants – B, Al, Ga, In – and anion dopants – F, Cl, Br, I – all with possible charge states of $q \in \{-2,-1,0,1,2\}$, were considered. At each Fermi level, the most favorable charge state for each defect is plotted in Figure 1 under Zn-rich and S-rich conditions for both cubic and hexagonal phases. According to these calculations, the aluminum dopant is the only one that forms a stable compound at Fermi levels close to the CBM, under Zn-rich conditions, in both phases. Otherwise, for all other dopants, the compounds formed are less favorable than the formation of ${V_{\text{Zn}}}^{-2}$, which is the strong driver of p-type behavior due to Fermi level pinning; this makes it difficult to push the Fermi level closer to the CBM (i.e. n-type doping)[39,43]. This is also consistent with the hybrid functional calculations of Varley and Lordi[1] for the cubic phase of ZnS. This effect is much less significant in buffer layers, such as CdS — making it easier to n-dope such materials[17]. The calculated formation energy values of ${V_{\text{Zn}}}^{-2}$ defects, when the Fermi level is at the CBM, are 0.107 eV in the cubic and -0.247 eV in the hexagonal phase — both of which are the lowest among the defects considered here. However, there is an uncertainty associated with the levels at which Al_{Zn} and V_{Zn} cross, as the calculated band gap with the HSE hybrid functional is 3.24 eV (3.29 eV), compared to the experimental value of 3.54 eV (3.91 eV) for the cubic (hexagonal) phases, respectively. It is recommended to have the growth environment as rich as possible in Zn, to reduce the possibility of the formation of zinc vacancies. Then, the formation of Al_{Zn} sites will result in an n-type semiconductor with high carrier concentration and electrical conductivity.

On the other hand, under S-rich conditions, F_{S} forms more favorably compared to other anion dopants. However, it is only more favorable than the hole inducer, ${V_{\text{Zn}}}^{-2}$, deep inside the band gap, which results in low carrier concentrations. Therefore, considering only the stability analysis, Al is the most promising candidate.

Our *ab initio* thermodynamic calculations for ZnS alloyed with Al (shown in Figure 2) and other dopants at different concentrations show that once alloyed, the hexagonal phase is more thermodynamically favorable than the cubic phase, even at room temperature. The preference for the hexagonal phase has previously been reported for Co-doped ZnS[22]. It is also expected that, upon doping, a mixture of the two phases forms[20], which may be the main reason for the lower-than-expected conductivity measured for polycrystalline samples[15–18]. This phenomenon can be explained with the calculations presented in Figure 2, which show the transition between cubic and hexagonal phases between 600-800 K. We also present in Supplementary Information, a comparison between Al:ZnS and Al:ZnO, where we show why Al is more easily integrated in the ZnO lattice compared to ZnS – the lack of two-phase complexity in ZnO and forming short/strong/ionic bonds between Al and O in AZO. Nevertheless, AZS is still a viable TCM, particularly if efforts are made to preferentially synthesize the hexagonal phase at lower temperatures.

Table 2 Change in the lattice constant $|\mathbf{a}|$ of cubic and hexagonal ZnS, upon alloying with Al at different dopant concentrations. Incorporation of Al increases the ZnS lattice constant at all dopant compositions.

x in $\text{Al}_x\text{Zn}_{1-x}\text{S}$ (%):	3.125	6.25	9.375	12.5
Cubic (%)	0.27	0.63	0.97	1.26
Hexagonal (%)	-	1.01	-	1.20

Finally, the incorporation of Al in the ZnS lattice, whether cubic or hexagonal, results in an increases in the lattice constants. This is evident upon *ab initio* geometry optimization of AZS at different dopant concentrations, as presented in Table 2. The hexagonal phase tends to expand more at lower concentrations of Al, but ultimately is limited to a net 1.25% increase in the lattice constant.

3.2 Electronic properties

Candidate TCMs must also possess good optical transparency and electrical conductivity. To qualitatively assess these properties, we first calculate the band gap and effective mass of ZnS alloyed with various elements, and summarize the results in Table 3. As shown, most of the alloying elements, regardless of whether they are cations or anions, increase the electron effective mass of ZnS, particularly at high dopant concentrations. Of these, $\text{ZnS}_{1-x}\text{F}_x$ at 3.125%, and $\text{B}_x\text{Zn}_{1-x}\text{S}$, $\text{ZnS}_{1-x}\text{Cl}_x$, and $\text{ZnS}_{1-x}\text{Br}_x$ at 9.375% doping, show a significant increase in their effective masses, which is detrimental to the conductivity. The effect of dopants on effective mass can be attributed to the hybridization of the dopant *s*-orbital with the Zn-*s* and S-*s* orbitals at the CBM. This can also be seen in the density of states (DOS) plots available in Supplementary Information. The DOS plot also shows that Al does not introduce mid-gap states, which can be highly detrimental to the optical absorption. It should be noted that here we simulate substitutional doping[17,43,44]. To evaluate the dependence of the calculated effective mass on the doping site, we calculated this property for all 16 Zn sites in 6.25% Al-doped hexagonal ZnS (i.e., $\text{AlZn}_{15}\text{S}_{16}$), and we obtained an average effective mass of 0.175449 ± 0.0000124. The small deviation shows that calculating the effective mass at the selected sites can be a good representation of substitutional doping at the corresponding doping percentage. On the other hand, Table 3 shows that alloying ZnS with Al gives the smallest reduction in the band gap with no mid-gap states present, even at high concentrations, which may preserve the optical transparency of the host material. Even at the high dopant concentration of 12.5%, the calculated band gap for AZS is 2.92 eV, which is only 0.32 eV lower than the calculated value for undoped ZnS. For comparison, Cl doping of 9.375% into the

This journal is © The Royal Society of Chemistry [year]

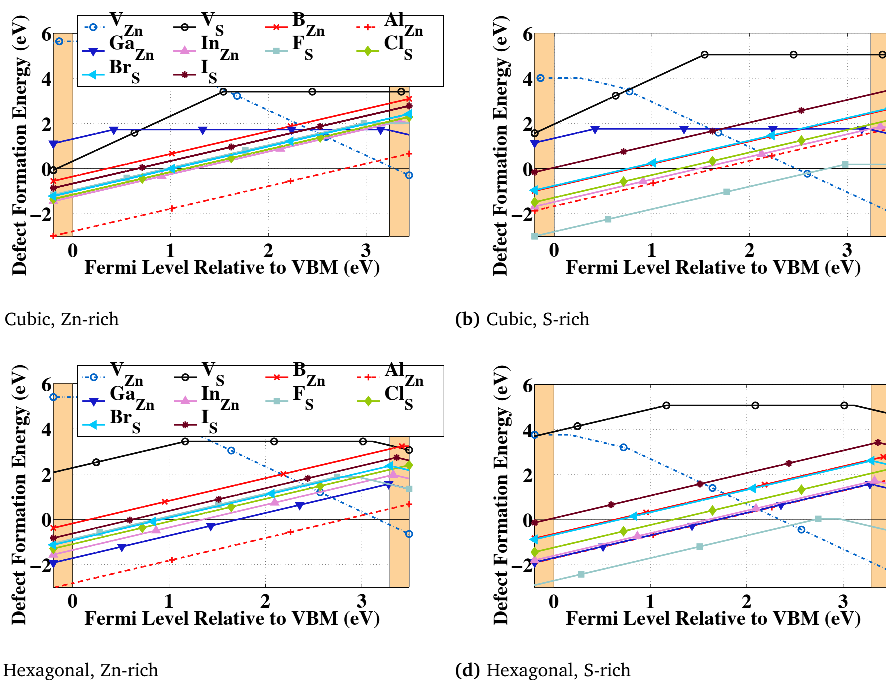

(a) Cubic, Zn-rich

(b) Cubic, S-rich

(c) Hexagonal, Zn-rich

(d) Hexagonal, S-rich

Fig. 1 Formation energy of defects in cubic ((a) and (b)) and hexagonal ((c) and (d)) phases of ZnS. At each Fermi level, the most favorable charge state is plotted. The slope of the lines is equal to the charge of the defect (e.g., +1 for ${Al_{Zn}}^{+}$). The Fermi level (abscissa) ranges from 0 at the VBM, up to the calculated band gap (from the HSE hybrid functional) of 3.24 eV (3.29 eV) for the cubic (hexagonal) ZnS.

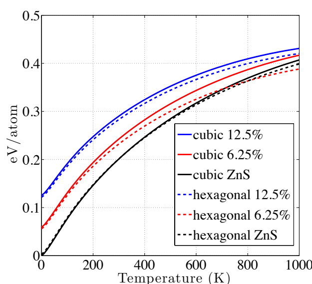

Fig. 2 *ab initio* thermodynamic calculations for both cubic and hexagonal ZnS alloyed with Al with different concentrations. The hexagonal phase is more favorable than the cubic phase for doped ZnS. The Gibbs energy (ordinate) includes the zero temperature contributions, which are calculated using DFT, and the vibrational entropy, which is calculated using DPFT and the Phonopy code.

ZnS lattice results in a 1.16 eV reduction in the band gap. Thus, AZS is likely to remain transparent even as its conductivity improves over undoped ZnS.

As reported in Table 3, the band gap of ZnS slightly decreases upon introduction of dopants. However, the question is whether the increase in electron concentration overcomes both the increase in effective mass (and concomitant decrease in mobility) to yield a net increase in conductivity, and the reduction in band gap that decreases the optical transparency. AMSET is thus used to calculate the electronic transport properties at relevant temperatures. Since the unit cell of ZnS is relatively small, we also perform *GW* band structure calculations to obtain the correct band shape; this results in a calculated effective mass closer to experimental measurements (see Table 3). We present here the AMSET calculations for the hexagonal phase of AZS. The calculated mobilities of ZnS at electron concentrations of $n \in \{10^{14}, 10^{18}, 10^{19}, 10^{20}, 10^{21}\}$ cm^{-3}, over the temperature range of $50-600$ K, are shown in Figure 3a. These concentrations were chosen to best match the experimentally-available conductivity data at $n = 1.0 \times 10^{14}$ cm^{-3} [46]. Furthermore, higher concentrations are also considered for higher dopant concentrations or higher ionization. We acknowledge that the Al dopant concentration and the carrier concentrations are not independent; however, as the band structures of Al-doped systems are very similar, we do consider different hypothetical carrier concentrations for a selected Al dopant concentration, in order to show the behavior of AZS at different dopant concentrations. Carrier concentrations of $8.8 \times 10^{18} - 1.1 \times 10^{21}$ cm^{-3} have been reported for doped ZnS [15], and AZS is even more likely to achieve the high-

Table 3 Calculated band gap and effective mass of undoped ZnS and that alloyed with B, Al, Ga, In, F, Cl, Br and I. The effective mass of the alloyed systems has is calculated using the PBE functional only, while the band gap is calculated using the HSE hybrid functional and compared to the 3.24 eV value calculated for undoped ZnS.

	Effective mass		Band gap (eV)	
ZnS (exp.[45])	0.31		3.80	
Cubic ZnS (GW)	0.25		3.69	
Cubic ZnS (DFT)	0.171		2.02	
Hexagonal	0.173		2.07	
$M_xZn_{1-x}S$	3.125 %	9.375 %	3.125 %	9.375 %
B	0.165	0.310	3.09	2.03
Al	0.171	0.203	3.11	2.46
Ga	0.173	0.229	2.91	1.90
In	0.171	0.191	2.85	1.98
$ZnS_{1-x}A_x$	3.125 %	9.375 %	3.125 %	9.375 %
F	0.184	0.216	2.75	2.60
Cl	0.167	0.353	3.07	2.08
Br	0.164	0.292	3.06	1.64
I	0.163	0.240	3.04	1.77
$Al_xZn_{1-x}S$	6.25 %	12.5 %	6.25 %	12.5 %
Cubic	0.167	0.173	3.04	2.92
Hexagonal	0.176	0.178	3.09	2.92

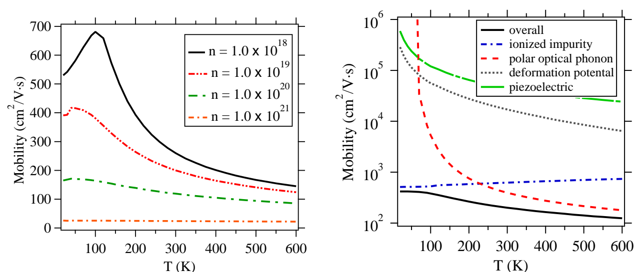

(a) Mobility at different n and T

(b) Scattering mechanisms at $n = 10^{18}$ cm^{-3}

Fig. 3 Calculated mobility of 6.25% Al-doped hexagonal ZnS from the band structure calculated *ab initio* using DFT. (a) The reduction in the mobility at higher electron concentrations, n, as caused by ionized impurity scattering. (b) Importance of different limiting scattering mechanisms at low temperatures.

est carrier concetnration because Al is, as shown in Figure 1, marginally more energetically favorable than other dopant candidates. It should be noted that at very high carrier concentrations the reflectivity of the material can be detrimental to its optical properties[47]. However, the calculated electrical conductivity of AZS is still high, even at relatively lower carrier concentrations of $n = 10^{19}$ and 10^{20}. As shown in Figure 3a, the decrease in the mobility due to the increase in carrier concentration (i.e., ionized impurity scattering) asymptotes as the electron concentration reaches 1.0×10^{20} cm^{-3}. After that, ionized impurities are the main limiting scattering mechanism at all temperatures, and the mobility monotonically decreases with increasing concentrations. At $n = 1.0 \times 10^{21}$ cm^{-3}, the mobility is almost constant at all temperatures, with no scattering contribution from polar optical phonons. The effect of each scattering mechanism on the overall mobility can be seen in Figure 3b at $n = 1.0 \times 10^{18}$ cm^{-3}, where ionized impurities are the limiting scattering mechanism at low temperatures, and polar optical phonons are the limiting scattering mechanism at higher temperatures.

The calculated mobility by AMSET is sensitive to the calculated band shape – particularly closer to the CBM, which dictates the effective mass. Therefore, we also report the calculated effective mass in Table 3. However, it should be noted AMSET does not use the effective mass as a fitting parameter; rather, its results are merely sensitive to this value. As reported in Table 3, DFT underestimates the band gap and the effective mass. Since we need large supercells for simulating the process of alloying in ZnS, *GW* calculations are very computationally demanding for these large systems, and thus, only DFT is used for these supercell calculations.

The increase in effective mass as a result of alloying is inevitable, as shown in Table 3. However, aluminum does not significantly reduce the band gap, nor does it significantly increase the effective mass. Therefore, among the candidates studied here, aluminum makes an excellent dopant with high solubility, stability, and optical transparency (around 75%[48]); in particular, the 6.25% dopant concentration results in the highest conductivity and the lowest reduction in the band gap. Therefore, we propose 6.25% as the optimal dopant concentration, which is consistent with the 6% reported by Prathap et al.[19], even though the cubic phase was studied there (see Table 3; 6.25% Al is also optimal for the cubic phase). AZS thus exhibits relatively high electrical conductivity even though it is an inexpensive transparent conductor.

The combined effect of the change in the band structure and carrier concentration is taken into account by calculating the electrical conductivity as $\sigma = nq\mu$, where q is the charge of an electron and μ is the mobility. According to Figure 4, the conductivity can increase up to 6 orders of magnitude by doping ZnS with 6.25% Al. The increase in conductivity is primarily due to the increase in the carrier concentration that counteracts the decrease in mobility due to ionized impurity doping. For example, in 6.25% Al, the 505,000-fold increase in the conductivity at $n = 10^{21}$ cm^{-3}, compared to undoped ZnS at $n = 10^{14}$ cm^{-3}, is the product of the 10,000,000-fold increase in carrier concentration and the 0.0505-fold decrease in mobility caused by alloying. Meanwhile, the calculated conductivity of 6.25% Al-doped ZnS at 300 K is 3830 S$\cdot$cm^{-1} at $n = 1.0 \times 10^{21}$cm^{-3} and 1905 S$\cdot$cm^{-1} at $n = 1.0 \times 10^{20}$ cm^{-3}. This is comparable to the reported conductivity of $1000 - 5000$ S$\cdot$cm^{-1} for AZO synthesized with $n = 0.5 - 1.0 \times 10^{21}$ cm^{-3} [49], but much higher than the corresponding values of 0.042 S$\cdot$cm^{-1} [19] and 10^{-3} S$\cdot$cm^{-1} reported for AZS films[48]. Again, we believe this discrepancy can be primarily attributed to the presence of the polycrystallinity and the mixed phases present in the experimentally synthesized samples discussed here, and secondarily due to the errors in the DFT calculations reflected in the underestimation of the effective mass and concomitant overestimation of the calculated conductivity at $n = 10^{14}$ cm^{-3} (Figure 4). A more accurate description of the band structure of alloyed ZnS would enable us to obtain the theoretical limits for conductivity in single-crystalline AZS. Nevertheless, the main findings outlined in this work confirm the viability of

This journal is © The Royal Society of Chemistry [year]

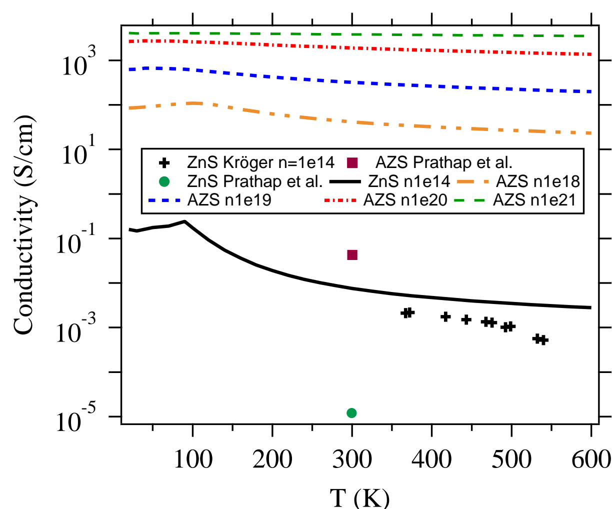

Fig. 4 Conductivity of undoped (black) and hexagonal AZS (6.25% Al) at different carrier concentrations, as calculated using AMSET. The overestimation of the conductivity by AMSET is related to the underestimation of the effective mass (overestimation of group velocities) in DFT calculations. Prathap et al.[46] results are for polycrystalline cubic samples with unreported carrier concentrations; hence, only the 300K conductivity values are plotted here.

aluminum-doped ZnS, at dopant concentrations around 6%, as a high-performing transparent conducting material.

4 Conclusion

We use hybrid density functional calculations to obtain formation energies and band gaps of ZnS alloyed with B, Al, Ga, In, F, Cl, Br and I, and calculate the effective mass and electrical mobility and conductivity of these compounds at various dopant concentrations, temperatures, and carrier concentrations, to identify potential high-performing n-doped ZnS for transparent conducting applications. We found that aluminum is soluble in ZnS, and more significantly, leads to an increase in the electrical conductivity with minimal reduction in the band gap. Also, our calculations show that upon doping, the hexagonal phase of ZnS is more thermodynamically favorable to form than the cubic phase, which may be significant in guiding further experimental efforts in synthesis and characterization. We believe that AZS is the best candidate for an n-type ZnS based transparent conductor, with 6.25% Al-doped ZnS exhibiting a calculated conductivity of 3830 $S \cdot cm^{-1}$ at $n = 1.0 \times 10^{21}$ cm^{-3} at 300 K. The methodology outlined should also be broadly applicable to the design of compound semiconductors for optoelectronic applications.

Acknowledgment This research is based upon work supported by the Solar Energy Research Institute for India and the U.S. (SERIIUS) funded jointly by the U.S. Department of Energy subcontract DE AC36-08G028308 (Office of Science, Office of Basic Energy Sciences, and Energy Efficiency and Renewable Energy, Solar Energy Technology Program, with support from the Office of International Affairs) and the Government of India subcontract IUSSTF/JCERDC-SERIIUS/2012 dated 22nd Nov. 2012. This work used the Extreme Science and Engineering Discovery Environment (XSEDE), which is supported by National Science Foundation grant number OCI-1053575. The authors also thank Joel Ager and K. R. Balasubramaniam for helpful discussions during the preparation of this manuscript.

References

1 J. B. Varley and V. Lordi, *Applied Physics Letters*, 2013, **103**,.

2 C. J. Traverse, M. Young, S. Wagner, P. Zhang, P. Askeland, M. C. Barr and R. R. Lunt, *Journal of Applied Physics*, 2014, **115**,.

3 F. Maldonado and A. Stashans, *Journal of Physics and Chemistry of Solids*, 2010, **71**, 784 – 787.

4 M.-C. Jun, S.-U. Park and J.-H. Koh, *Nanoscale Research Letters*, 2012, **7**, 1–6.

5 Y.-J. Choi and H.-H. Park, *J. Mater. Chem. C*, 2014, **2**, 98–108.

6 J. Clatot, G. Campet, A. Zeinert, C. LabrugÃÍre, M. Nistor and A. Rougier, *Solar Energy Materials and Solar Cells*, 2011, **95**, 2357 – 2362.

7 K. Ellmer, *Journal of Physics D: Applied Physics*, 2001, **34**, 3097.

8 M. L. Grilli, A. Sytchkova, S. Boycheva and A. Piegari, *physica status solidi (a)*, 2013, **210**, 748–754.

9 H. Agura, A. Suzuki, T. Matsushita, T. Aoki and M. Okuda, *Thin Solid Films*, 2003, **445**, 263 – 267.

10 A. Janotti and C. G. Van de Walle, *Phys. Rev. B*, 2007, **76**, 165202.

11 G. Hautier, A. Miglio, G. Ceder, G.-M. Rignanese and X. Gonze, *Nat. Commun.*, 2013, **4**, 3292.

12 A. M. Diamond, L. Corbellini, K. R. Balasubramaniam, S. Chen, S. Wang, T. S. Matthews, L.-W. Wang, R. Ramesh and J. W. Ager, *Phys. Status Solidi A*, 2012, **209**, 2101–2107.

13 R. Woods-Robinson, J. K. Cooper, X. Xu, L. T. Schelhas, V. L. Pool, A. Faghaninia, C. S. Lo, M. F. Toney, I. D. Sharp and J. W. Ager, *Advanced Electronic Materials*, 2016, n/a–n/a.

14 C. Wang, G. Yang, T. Zhang, H. Liu, Y. Han, J. Luo, C. Gao and G. Zou, *Diamond and Related Materials*, 2003, **12**, 1548 – 1552.

15 B. Long, S. Cheng, H. Zhou, J. Liao, H. Zhang, H. Jia and H. Li, *ECS Solid State Letters*, 2014, **3**, P140–P143.

16 A. Jrad, T. Nasr and N. Turki-Kamoun, *Journal of Materials Science: Materials in Electronics*, 2015, **26**, 8854–8862.

17 J. Liao, S. Cheng, H. Zhou and B. Long, *Micro & Nano Letters*, 2013, **8**, 211–214(3).

18 K. Nagamani, N. Revathi, P. Prathap, Y. Lingappa and K. R. Reddy, *Current Applied Physics*, 2012, **12**, 380 – 384.

19 P. Prathap, N. Revathi, Y. Subbaiah, K. R. Reddy and R. Miles, *Solid State Sciences*, 2009, **11**, 224 – 232.

20 A. E. Hichou, M. Addou, J. L. Bubendorff, J. EbothÃľ, B. E. Idrissi and M. Troyon, *Semiconductor Science and Technology*, 2004, **19**, 230.

21 Z. K. Heiba, N. Imam and M. B. Mohamed, *Materials Science in Semiconductor Processing*, 2015, **34**, 39 – 44.

22 K. Deepa, A. Dhanya and T. Remadevi, *Journal of Materials Science: Materials in Electronics*, 2014, **25**, 1214–1221.

23 A. Faghaninia, J. W. Ager and C. S. Lo, *Phys. Rev. B*, 2015, **91**,

235123.
24 D. L. Rode, in *Semiconductors and semimetals*, Academic Press, 1975, vol. 10, ch. 1, Low-Field Electron Transport.
25 P. Hohenberg and W. Kohn, *Phys. Rev.*, 1964, **136**, B864–B871.
26 W. Kohn and L. J. Sham, *Phys. Rev.*, 1965, **140**, A1133–A1138.
27 G. Kresse and J. Hafner, *Phys. Rev. B*, 1993, **47**, 558–561.
28 G. Kresse and J. Hafner, *Phys. Rev. B*, 1994, **49**, 14251–14269.
29 G. Kresse and J. Furthmüller, *Comput. Mater. Sci.*, 1996, **6**, 15 – 50.
30 G. Kresse and J. Furthmüller, *Phys. Rev. B*, 1996, **54**, 11169–11186.
31 J. P. Perdew, K. Burke and M. Ernzerhof, *Phys. Rev. Lett.*, 1996, **77**, 3865–3868.
32 P. E. Blöchl, *Phys. Rev. B*, 1994, **50**, 17953–17979.
33 G. Kresse and D. Joubert, *Phys. Rev. B*, 1999, **59**, 1758–1775.
34 G. Bergerhoff, R. Hundt, R. Sievers and I. Brown, *J. Chem. Inf. Model.*, 1983, **23**, 66–69.
35 A. Jain, S. P. Ong, G. Hautier, W. Chen, W. D. Richards, S. Dacek, S. Cholia, D. Gunter, D. Skinner, G. Ceder and K. A. Persson, *APL Materials*, 2013, **1**, 011002.
36 A. Togo, F. Oba and I. Tanaka, *Phys. Rev.. B*, 2008, **78**, 134106.
37 S. P. Ong, W. D. Richards, A. Jain, G. Hautier, M. Kocher, S. Cholia, D. Gunter, V. L. Chevrier, K. A. Persson and G. Ceder, *Computational Materials Science*, 2013, **68**, 314 – 319.
38 G. Makov and M. C. Payne, *Phys. Rev. B*, 1995, **51**, 4014–4022.
39 A. Faghaninia and C. S. Lo, *Journal of Physics: Condensed Matter*, 2015, **27**, 125502.
40 A. J. Jackson and A. Walsh, *Phys. Rev. B*, 2013, **88**, 165201.
41 Y. C. Cheng, C. Q. Jin, F. Gao, X. L. Wu, W. Zhong, S. H. Li and P. K. Chu, *Journal of Applied Physics*, 2009, **106**,.
42 X. Sun, A. Faghaninia, M. Stoica and C. S. Lo, *Journal of Physics: Condensed Matter (in revision)*, 2016.
43 L. Bjerg, G. K. H. Madsen and B. B. Iversen, *Chem. Mater.*, 2012, **24**, 2111–2116.
44 C. G. Van de Walle, *Phys. Rev. Lett.*, 2000, **85**, 1012–1015.
45 H. E. Ruda and B. Lai, *Journal of Applied Physics*, 1990, **68**, 1714–1719.
46 F. Kröger, *Physica*, 1956, **22**, 637 – 643.
47 R. G. Gordon, *MRS Bulletin*, 2000, **25**, 52–57.
48 K. Nagamani, P. Prathap, Y. Lingappa, R. Miles and K. R. Reddy, *Physics Procedia*, 2012, **25**, 137 – 142.
49 T. Minami, H. Sato, K. Ohashi, T. Tomofuji and S. Takata, *Journal of Crystal Growth*, 1992, **117**, 370 – 374.

This journal is © The Royal Society of Chemistry [year]